

EVERT NASEDKIN

SIMULATED INSTRUMENTAL CONSTRAINTS
ON SUB-STELLAR ATMOSPHERIC
RETRIEVALS FOR THE JAMES WEBB SPACE
TELESCOPE'S MID-INFRARED
INSTRUMENT.

Evert Nasedkin

*Simulated Instrumental Constraints on Sub-Stellar Atmospheric Retrievals for the
James Webb Space Telescope's Mid-Infrared Instrument.*

Copyright © 2020

TITLEBACK

This document was written with \LaTeX on Ubuntu using ArsClassica, designed by André Miede.

CONTACTS

✉ evertn@student.ethz.ch



Eidgenössische Technische Hochschule Zürich
Swiss Federal Institute of Technology Zurich

Declaration of originality

The signed declaration of originality is a component of every semester paper, Bachelor's thesis, Master's thesis and any other degree paper undertaken during the course of studies, including the respective electronic versions.

Lecturers may also require a declaration of originality for other written papers compiled for their courses.

I hereby confirm that I am the sole author of the written work here enclosed and that I have compiled it in my own words. Parts excepted are corrections of form and content by the supervisor.

Title of work (in block letters):

Authored by (in block letters):

For papers written by groups the names of all authors are required.

Name(s):

First name(s):

With my signature I confirm that

- I have committed none of the forms of plagiarism described in the '[Citation etiquette](#)' information sheet.
- I have documented all methods, data and processes truthfully.
- I have not manipulated any data.
- I have mentioned all persons who were significant facilitators of the work.

I am aware that the work may be screened electronically for plagiarism.

Place, date

Signature(s)

For papers written by groups the names of all authors are required. Their signatures collectively guarantee the entire content of the written paper.

ACKNOWLEDGEMENTS

—

ABSTRACT

Following its launch in 2021, the James Webb Telescope will provide the best infrared observations of exoplanets and brown dwarfs to date. In particular, the Mid-Infrared Instrument (MIRI), will allow for medium resolution spectroscopy across a wide wavelength band, from $4.9\text{-}28.8\mu\text{m}$. This will allow us to derive atmospheric properties of objects at lower temperatures than currently possible. MIRI's medium resolution spectrometer (MRS) is an integrated field unit that will perform these observations, providing both spatial and spectral information about targets. Understanding the instrumental effects is critical to analyzing data from MIRI. With that in mind, the MIRISIM instrumental simulator was developed to provide observational simulations of the various sub instruments of MIRI.

This thesis improves the implementation of a thin-film fringing model for point sources to MIRISIM, considering how the fringing effect from the detector layers varies with position. Fringing is a periodic, wavelength dependent effect, and thus has a strong impact on any spectroscopic observations. A comparison to the existing model was made, demonstrating the necessity of considering this effect when analyzing data. We will improve the fringing removal by identifying the point source location from the constructed data cube, and select the correct fringe flat for removal.

Understanding the instrumental effects is key to quantifying the ability of MIRI to derive atmospheric properties. Existing literature has considered the NIRCAM instrument and the MIRI Low-Resolution Spectrometer, but to date no retrieval studies have been performed using MIRISIM, or for the MIRI MRS, though it is critical to extend wavelength coverage to improve the results of an atmospheric retrieval. Model atmospheres will be generated using PetitRadTrans, and processed using MIRISIM and the JWST pipeline to produce a mock observation. An atmospheric retrieval will be performed, demonstrating to what extent MIRI will be able to retrieve atmospheric parameters such as temperature, pressure and composition. The posterior distributions of these parameters are compared with and without the fringing removal, again demonstrating the importance of correcting for this effect.

CONTENTS

1	INTRODUCTION	1
1.1	Exoplanets	1
1.2	Brown Dwarfs	3
1.2.1	Physics	4
1.2.2	Observational Properties	4
1.3	Motivation	4
1.3.1	Current Status of Atmospheric Characterization	4
1.3.2	JWST Studies	4
1.3.3	Biosignatures and Future Missions	4
1.4	Thesis Overview	4
2	MIRI: THE MID-INFRARED INSTRUMENT	5
2.1	The James Webb Space Telescope	5
2.2	MIRI	6
2.3	The Medium Resolution Spectrograph	6
2.3.1	Coordinates	7
2.3.2	Integrated Field Spectroscopy	7
2.3.3	Optical Systems	7
2.3.4	Detectors	8
2.4	Observations	8
2.4.1	Dithering	8
2.4.2	Exposure time calculations	8
3	FRINGING EFFECTS IN MIRI	11
3.1	Fringing	11
3.2	MIRISIM	12
3.2.1	Architecture	12
3.2.2	Data Products	13
3.2.3	Instrumental effects	13
3.2.4	Fringing	13
3.2.5	Fringing Implementation	14
3.3	JWST Pipeline	14
3.3.1	Stage 1 Processing	14
3.3.2	Stage 2 Processing	14
3.3.3	Cross-Correlation	15
3.3.4	Residual Statistics	16
3.4	Fringing Results	16
3.4.1	Effects of fringing on spectral extraction	17
4	ATMOSPHERIC RETRIEVALS	19
4.1	Atmospheric Modeling	19
4.1.1	petitRADTRANS	19
4.2	Bayesian methods	21
4.2.1	MCMC	21
4.2.2	Nested Sampling	21
4.2.3	multinest	21
4.2.4	Prior choice	21

	4.2.5	Bayesian Model Selection	21
4.3		Targets	21
	4.3.1	Atmospheric Parameters	21
	4.3.2	petitRadTrans	21
4.4		Results	21
	4.4.1	Posterior Distributions	21
5		CONCLUSIONS	23
A		APPENDICES	25
	A.1	Package Requirements	25

Since the first detection of a planet around a sun-like star (Mayor1995) the field of exoplanets has evolved rapidly. Thousands of companions have been identified using the radial velocity and transit detection methods, and a handful have been imaged directly using both ground and space based observatories. In the last decade, many advances have been made that allow us to begin to characterize the properties of a few of these planets using spectroscopy. With the launch of the James Webb Space Telescope (JWST) in 2021, and the dawn of the era of extremely large telescopes, we will be able to peer deeper into these planets and further constrain atmospheric or geological properties, allowing us to answer questions about their formation history, climate, and even the prospects for habitability and life.

JWST will operate in near to mid infrared wavelengths, which will provide a new window into studying the atmospheres of exoplanets and brown dwarfs. The Mid Infrared Instrument (MIRI) will provide unprecedented spectral resolution in the mid infrared, allowing for the measurement of composition, pressure and temperature. Novel instrumentation does not come without challenges. Optical and instrumental effects will constrain the ability to which we can measure spectral features, which will ultimately limit the science that can be accomplished.

In this thesis, we will measure the impact of thin-film fringing in the layers of the detectors in the MIRI Medium-Resolution Spectrometer on measurements of atmospheric parameters of brown dwarfs and exoplanets. This will provide a baseline for determining the level of correction necessary to minimize the impact of fringing, as well as providing a first look into the ability of the MRS to characterize atmospheres.

1.1 EXOPLANETS

The last quarter century of observations has revealed the diversity of exoplanets and extra-solar systems. Both the architecture and individual planetary characteristics vary greatly when compared to each other, as well as to our own solar system. From the hot Jupiters initially found by Mayor and Queloz (Mayor1995) to the thousands of planets discovered by the Kepler mission, the variety in exoplanets has raised questions about their formation and development, as well as their present day structure, climate, and even prospects for life. Improvements to observational techniques have allowed us to improve our understanding of these planets. Secondary eclipse and transmission spectroscopy has opened the door to the study of planets in close orbits to their host stars, while emission spectroscopy of young planet has allowed for constraints on models of planet formation. Over the next decades, new instruments will be developed that improve sensitivity,

allowing us to study smaller, colder and fainter planets: with the ultimate goal of studying atmospheric and surface features of an earth-like planet.

Of particular interest are observable features that allow us to measure physical properties of exoplanets. The radial velocity (RV) method provides a measure of the planet mass, while a transit can constrain the radius. Already these properties tell us something about the overall structure of the planet. Spectroscopy can provide insight into the composition of the planet's atmosphere, as well as its temperature and pressure. These properties are linked to its age and location of formation in the circumstellar disk. The atmosphere, combined with the distance between the planet and its star determine the climate of the planet.

Direct Imaging

While the majority of exoplanet detections have been made using the radial velocity or transit techniques, direct imaging opens up the possibility of collecting light from the planet itself. This provides a window into the planet's atmosphere and surface. Most direct imaging to date has used near-to-mid infrared wavelengths, where the contrast between the thermal emission from the planet and the star is at a minimum. This has its drawbacks: we are so far only able to image young planets that have retained some of the heat from their formation.

Direct imaging can make use of both ground and space based observatories. However, the high spatial resolution required drives the need for a large primary mirror, limiting the possibilities of space-based telescopes. On the other hand, atmospheric turbulence necessitates the use of an adaptive optics equipped facility to observe from the ground. Atmospheric absorption due to telluric lines (absorption lines of Earth's atmosphere) also restrict infrared observations to narrow bands.

In addition to the requiring high spatial resolution, it is also challenging to separate the light emitted by the planet from that of the star. Imaging techniques such as Angular Differential Imaging (ADI) (Marois2007) and Reference Differential Imaging (RDI) (Lefreniere2009; Soummer2012) provide methods for reducing the stellar point-spread-function (PSF). Coronagraphs are optical elements which suppress the stellar PSF through self-destructive interference or physical occultation, depending on the position in the optical path. The difference in spectra between the planet and the star can also be used to separate the two sources.

Presently, 10m class telescopes such as the Very Large Telescope (VLT) in Paranal, Chile or the Gemini Observatory split between Hawaii and Chile provide the best combination of resolution and instrumentation to perform direct imaging of exoplanets. The NACO instrument at the VLT provided the first image of an exoplanet in 2004 (Chauvin2004). These observatories are among those equipped with an adaptive optics system, coronagraphic instrumentation and near to mid infrared imaging and spectroscopic capabilities to directly image exoplanets, with several exemplar systems becoming standard objects of interest. The parameters of some directly imaged exoplanets are summarized in table 1

(Beichman2019) (Lagage2015) (Macintosh2006) (Macintosh2015)

Name
2M1207b
β Pic b
HR8799b
HR8799c
HR8799d
HR8799e
Fomalhaut b
2M J044144b
LkCa 15b
HD 95086b
Gliese 504b
51 Eridani b
PDS 70b
PDS 70c

Table 1: Summary of directly imaged planet parameters **Bowler2016** and references therein.

Beta Pictoris b

Discovered in 2008 (**Lagrange2009**), β Pic b is one of the most well-studied exoplanet systems (**Quanz2010; Chilcote2015; Chilcote2017; Hoeihmakers2018**). Due to its young age of 23 ± 3 Myr (**Mamajek2014**) and high mass of $12.9 M_J$ (**Chilcote2015**) it remains hot, between 1590K and 1847K (**Nowak2019**). Combined with its typically wide separation on its 9.2AU orbit (**Chauvin2012**), this allows for relatively easy imaging and spectroscopy in the near infrared. Recent RV observations indicate the possibility of an additional planet at 2.3 AU (**Lagrange2019**).

The quantity and quality of spectral data for β Pic b has allowed for the study and characterization of its atmosphere: measurements of its metallicity and C/O ratio can trace the formation history of the planet (**Chilcote2017; Nowak2019**). It also provides insight into its current atmospheric structure and composition, which can in turn inform models of exoplanet atmospheres.

HR 8799 System

PDS 70 b,c

1.2 BROWN DWARFS

(**Oliveira**) (**Helling2014**)(**Cooper2014**) (**Madhusudhan2018a**) (**Burrows2003**) (**Marley2014**) (**Manjavacas2014**) (**Biller2017**) (**Faherty2018**) (**Morley2014**)

1.2.1 Physics

1.2.2 Observational Properties

T-Type

L-Type

Y-Type

1.3 MOTIVATION

1.3.1 Current Status of Atmospheric Characterization

(Kreidberg2018)(Biller2018) (Bozza) (Danielski2018) (Madhusudhan2016)

Transmission Spectroscopy

(Lee2012) (MacDonald2017) (Madhusudhan)

Emission Spectroscopy

1.3.2 JWST Studies

(Beichman2019)

1.3.3 Biosignatures and Future Missions

1.4 THESIS OVERVIEW

2

MIRI: THE MID-INFRARED INSTRUMENT

MIRI is an instrument that will provide unique capabilities for studying exoplanets and other cold and distant objects. This chapter will provide a detailed overview of the technical details and capabilities of the instrument. A complete description of MIRI is provided in (**MIRI1**; **MIRI2**; **10.1086/6822554**; **MIRI4**; **MIRI5**; **MIRI6**; **MIRI7**; **MIRI8**; **MIRI9**)

2.1 THE JAMES WEBB SPACE TELESCOPE

JWST is a 6.5m space based observatory built in collaboration between NASA, ESA and CSA that will be located in a halo orbit at the L2 Earth-Sun Lagrange point. As the successor to the Hubble Space Telescope and the Spitzer Space Telescope, it will provide a new perspective for infrared astronomy. It is currently scheduled to launch in March 2021.

James Webb is fully optimized for infrared astronomy. To reduce instrumental thermal background, the entire telescope will operate at cryogenic temperatures. A large sun-shield will help block solar infrared radiation. The lightweight beryllium mirrors are coated in gold to maximize reflectivity out to the mid infrared.

Of key interest to exoplanet science is the both the sensitivity and spatial resolution of the instrument. With its 6.5m primary, JWST will have a spatial resolution from 0.01" at 0.6 micron to 0.92" at 29 micron. The increase in sensitivity is due in part to the larger collecting area, but also to advances in detector technology since the previous generation of infrared observatories. For example, the MIRI instrument will have a minimum detectable flux of 0.13 μ Jy at 5.6 micron, or roughly a factor of 1000 better than what was possible with the Spitzer Space Telescope (**MIRI9**).

There are four primary instruments that constitute the Integrated Science Instrument Module (ISIM). Near-Infrared Camera (NIRCam), which provides imaging with coronagraphic capabilities from 0.6-5 micron. The Near-Infrared Spectrograph (NIRSpec) provides fixed slit and integrated field unit spectroscopy capable of analyzing multiple objects simultaneously, and operates in the same wavelength range as NIRCam. The Fine Guidance Sensor/ Near-Infrared Imager and Slitless Spectrograph (FGS/NIRISS) allows for low and medium resolution spectroscopy with high photometric stability, as well as aperture masking interferometry. The final instrument, MIRI, is the subject of this thesis.



Figure 1: The James Webb Space Telescope during integration of the telescope into the Spacecraft Element (**assembled**).

Subsystem
Imaging
4QPM Coronagraphic Imaging
Lyot Coronagraphic Imaging
Low Resolution Spectroscopy
Medium Resolution Spectroscopy

Table 2: Summary of MIRI observing modes.

2.2 MIRI

The Mid-Infrared Instrument (MIRI) provides imaging, fixed slit and integrated field spectroscopy between 4.8 and 28 micron (**Rieke2015**). It will operate at a temperature of 6.7K to reduce instrumental backgrounds over its wavelength range of 0.6-28.8 micron.

(**Kendrew2015**)

2.3 THE MEDIUM RESOLUTION SPECTROGRAPH

The Medium Resolution Spectrograph (MRS) consists of four integrated field spectrographs projected onto two detectors, covering 4.8-28 micron with a spectral resolution varying from $R=1700$ to $R=3500$.

(**Wells2015**)

Channel	Sub-band	Band	Detector	λ Range [μm]	FOV [as]	$\lambda/\Delta\lambda$
1	Short	1A	SW	4.83 - 5.82	3.46×3.72	3500
	Medium	1B		5.62 - 6.73	3.46×3.72	3500
	Long	1C		6.46 - 7.76	3.41×3.72	3300
2	Short	2A	SW	7.44 - 8.90	4.16×4.76	3000
	Medium	2B		8.61 - 10.28	4.16×4.76	3000
	Long	2C		9.94 - 11.87	4.12×4.76	3000
3	Short	3A	LW	11.47 - 13.67	6.00×6.24	2700
	Medium	3B		13.25 - 15.80	5.96×6.24	2300
	Long	3C		15.30 - 18.24	5.91×6.24	2300
4	Short	3A	LW	17.54 - 21.10	7.14×7.87	1700
	Medium	3B		20.44 - 24.72	7.06×7.06	1700
	Long	3C		23.84 - 28.82	6.99×7.87	1500

Table 3: Properties of the MIRI MRS channels (MIRI6).

2.3.1 Coordinates

There are three primary coordinate systems in use with JWST/MIRI-MRS, of which two will be relevant for this thesis, with the detector and local MRS coordinates described in Fig. 2 (Argyriou2020).

The detector coordinate grid is formed by counting x/y pixels, as well as the slice number. Each of the two MRS detectors is an array of 1032×1024 pixels, though only 1024 are photosensitive in the horizontal direction. Each image slice from the IFU appears as a curved stripe on the detector, though neighboring stripes on the detector do not correspond to neighbouring slices of the image.

The local MRS coordinate system is described in terms of α , β and λ . The continuous α coordinate is the along slice direction, while β is perpendicular and discrete, corresponding to the slice number. λ is the wavelength. Both α and λ are fit by a second order polynomial to account for along and across slice distortion (MIRI6). Each detector sub array has its own mapping to α, β, λ space, due to the differences in FoV, slice count, distortion and spectral resolution.

The third coordinate frame is the global coordinate system of JWST itself, V_1, V_2, V_3 . The V_1 coordinate refers to the symmetry axis of the telescope, V_3 points towards the foldable secondary mirror support structure strut. V_2 completes the coordinate system, being orthogonal to V_1 and V_3 . This coordinate system will not be used in this thesis.

2.3.2 Integrated Field Spectroscopy

2.3.3 Optical Systems

Channels, bands, etc ref:Chen2019

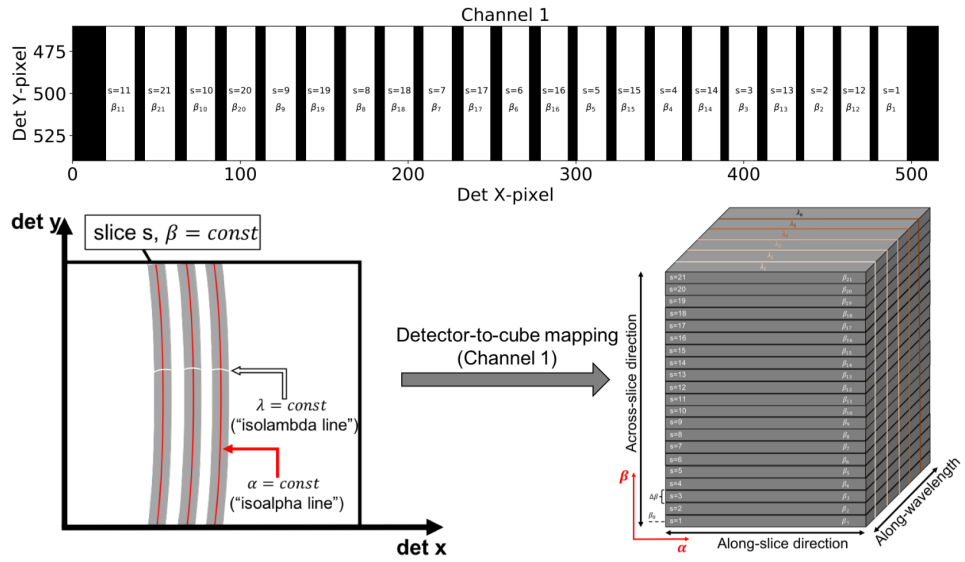


Figure 2: Description of the MRS detector (x, y, s) coordinate system to the local MRS (α, β, λ) cube coordinates. **Top:** Detector coordinates. Note that the consecutive stripe numbers s_i, s_{i+1} correspond to neighbouring image slices. **Bottom:** Description of the (invertible) detector-to-cube transformation (Argyriou2020).

Figure 3: Detector images of a spatially and spectrally flat calibration source for the SW detector (left) and LW detector (right).

2.3.4 Detectors

Readout Modes

2.4 OBSERVATIONS

2.4.1 Dithering

2.4.2 Exposure time calculations

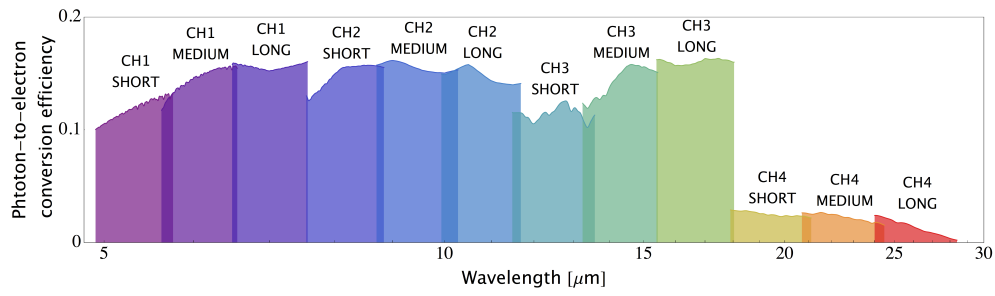


Figure 4: Average photon-to-electron conversion efficiencies for the MIRI MRS detectors

Understanding optical and instrumental effects is critical for creating accurate simulated observations and for characterizing systematics. These systematics and uncertainties in turn impact the potential science results from any instrument by biasing measurements, reducing the signal to noise ratio of measurements or by injecting non-physical signals and correlations. The aim of this chapter is to examine fringing in the MIRI detectors and how this effect is modeled in the instrumental simulator (MIRISIM).

3.1 FRINGING

Thin film interference occurs when light is coherently reflected at the boundary between two layers and interferes with the incident light. This is the principle on which Fabry-Pérot interferometers function. As we wish to determine the effect of fringing on the amplitude of the signal received by the detector, we are effectively interested in the transmittance of a series of Fabry-Pérot interferometers. Assuming an ideal plane-parallel optical cavity with a reflectance R at both boundaries, thickness D , and an angle θ at which the light travels within the cavity, we can compute the transmittance as:

$$T_c = \frac{1}{1 + \frac{4R}{(1-R)^2} \sin^2\left(\frac{\delta}{2}\right)} \quad (1)$$

Where the phase δ at half a wavelength ($\phi = \pi$), with wavenumber σ is:

$$\delta = 4\pi\sigma D \cos \theta - (\phi - \pi) \quad (2)$$

Systems with a spacing on the order of millimeters produces significant interference for infrared light (Lahuis2003).

The detectors of the MRS consist of several layers, as shown in Fig. 5, with a characteristic thickness of $500\mu\text{m}$, which results in significant (10%-30%) ‘fringing’ in a spectrally flat signal - visible in Fig. 3. While this is typical for infrared detectors such as those in the Spitzer Space Telescope (Lahuis2003) or in the Space Telescope Imaging Spectrograph on board HST (Malumuth2003), the sensitivity and spectral resolution of the MRS increase the significance of this issue. The MIRI consortium has stated that the error budget for all detector effects must be 3.3% or less. Present fringing corrections result in a 5% deviation from a photometrically accurate signal, and can introduce correlated noise which will degrade any measured spectrum. Therefore it is critical to examine the impact of fringing on a signal, the parameters that influence the fringing strength and phase, and possible solutions for fringe correction. While a more complete treatment of proposed fringe correction can be found in (Argyriou2020), this work will examine the implementation of fringing into the MIRI instrumental simulator and

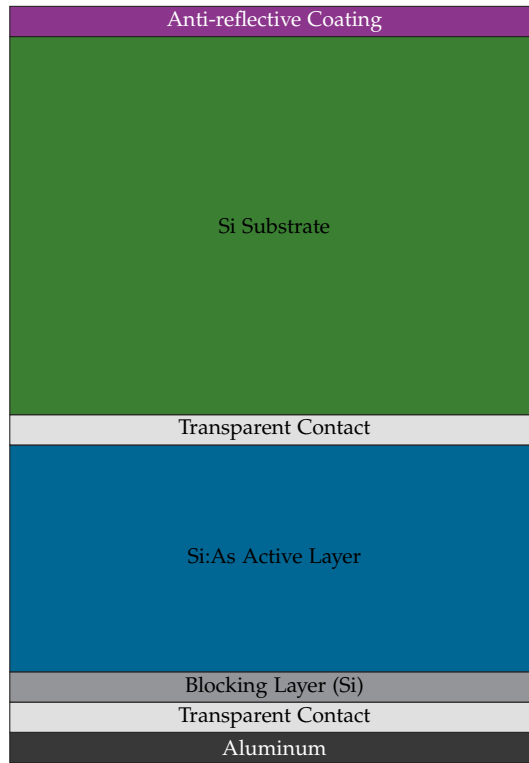


Figure 5: Layers of the MIRI MRS detectors. Note that thicknesses are not to scale (MIRI7).

address the current state of fringe correction in the JWST Data Calibration Pipeline.

Lahuis2018

3.2 MIRISIM

Consortium2018 Cossou2019 The MIRI instrument has been modeled in python as a program known as MIRISIM. This program takes in an astronomical ‘scene’ along with some configuration parameters to output a detector data product, similar to what will be produced by the actual instrument. This is relatively full-featured simulator, modelling the instrumental PSF, various noise sources and distortion maps, among other effects. While MIRISIM is functional for all of the MIRI sub-instruments, this report will only deal with the Medium-Resolution Spectrometer (MRS) sub instrument, described in section 2.3. The goal of this section is to describe the implementation and testing of an updated optical model of the ‘fringing’ effect - an optical effect caused by thin film interference from the multiple layers of the detector.

3.2.1 Architecture

SCENE - SEDs SIMULATOR PYSPECSIM

Figure 6

Table 4

3.2.2 Data Products

3.2.3 Instrumental effects

3.2.4 Fringing

Lahuis2003 VanderPlas2018 A key effect on spectral data is fringing, described in **ref:Argyriou2018**. MIRI uses a total of three Si:As impurity band conduction detector arrays, two of which are used by the MRS. These detectors consist of 7 layers, listed in table 4 and illustrated in Fig. 5.

If all of the parameters were known, this would be sufficient to numerically solve for the fringing pattern within MIRI. Unfortunately, uncertainties in the thickness in the detector layers, variations in the layer deposition thickness, and the uncertainty of transmittance and reflectance of the materials used at cryogenic temperatures prevents the implementation of such a numerical model.

Instead, we turn to calibration data taken to characterize the fringing pattern.

DESCRIBE CURRENT MODEL - GENERIC FRINGING

However, due to the dependance of fringing on the incident angle of the light, a single model of fringing is insufficient to describe the full effect. Therefore, we use data taken in XXXXXXXXXX at various points across the detector and quantify how this changes the extracted spectra after processing in the JWST pipeline.

DESCRIBE HOW THE DATA WAS TAKEN HERE. - Problems with point vs extended sources - multiple collection runs

Ultimately this data collection produced a series of 'fringe-flats' of an almost point like at various position across the detector and in each channel. We implemented a new routine into the pySpecSim portion of MIRISIM to read in the location of point sources within a scene, and apply the correct position dependent fringe flat. This implementation comes with several caveats: namely that the fringing model is not yet fully developed, so it can only be considered accurate for point sources located at the same (α, β) location as the source used to produce the fringe flat. Additionally, the source used to generate the data is not a true point source, nor are there fringe flats produced for the full MRS wavelength range. We stress that the goal of this testing is to demonstrate the significance of this effect to justify the need for a more complete model along with additional calibration data to constrain the detector layer parameters.

*FM Data**CV Data*

3.2.5 Fringing Implementation

3.3 JWST PIPELINE

Bushouse2015 Labiano-Ortega2016

3.3.1 Stage 1 Processing

3.3.2 Stage 2 Processing

Photometric Calibration

Photometric calibration is the process of removing detector and optical biases to ensure that the measured output corresponds to the true flux incident onto the telescope. This process occurs in the PHOTOM step of the JWST pipeline, and uses reference files which store per-pixel photon-to-electron conversion efficiencies to transform the count rate data product to a flux measurement. This corrects for the wavelength dependent bias shown in Fig. 4.

However, this step remains under development, and does not produce absolutely calibrated images. In particular, even using the most up to date reference files (v8D.04.00) there remains discontinuities between channels, and poorly calibrated slopes.

*Fringing correction***Carnall2017***Cube Building**Aperture Photometry*

Once the data from the pipeline has been transformed into a spectral cube, we can perform aperture photometry using the photutils package to extract a 1D spectrum of the source. For each frame in each sub-band the coordinates of the spaxel at which the peak flux is detected using photutils `find_peaks`, which provides the location for the center of a circular aperture. A radius of 5 spaxels is used to encompass the entire PSF for a point source. If the files have already been photometrically calibrated, measuring the flux requires just adding the flux from each spaxel within the defined radius for each frame. While optimal extraction techniques exist, given our known input signal and background, this procedure is adequate for producing a spectrum in each sub-band, which can then be combined into a single spectrum for all measured sub-band.

Unfortunately, due to the issues described above with the PHOTOM step of the JWST pipeline, the spectrum built using aperture photometry does not accurately reflect the input spectrum in slope or absolute photometry. Therefore, we correct the extracted spectrum channel by channel. We fit a cubic

polynomial to a median filtered copy of both the template spectrum and the extracted spectra. The cubic fit to the extracted spectra is subtracted from the data, and the fit to the template is added. Thus this procedure corrects the slope and median flux value, but does not affect high frequency noise or signals. Fig. 7 shows an example of the results of this procedure. We believe that this is a justified measure, as the errors with photometric calibration in the pipeline should be resolved before first light of the telescope.

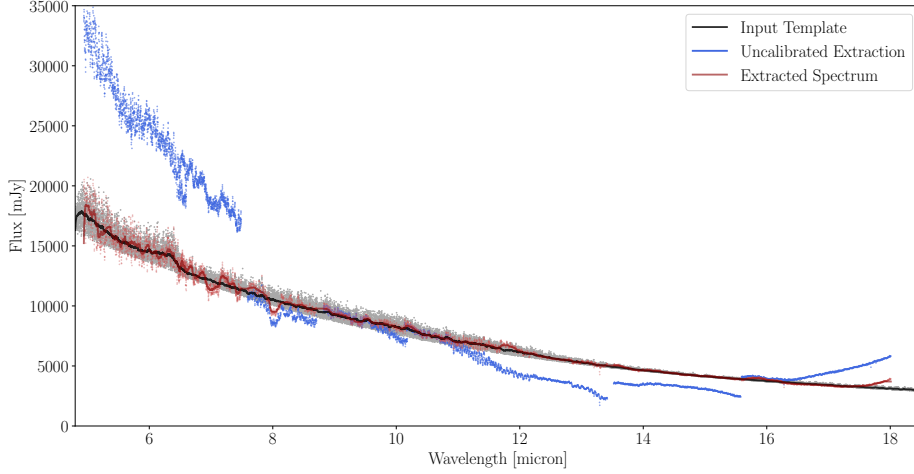


Figure 7: Comparison of an input spectrum generated using petitRadTrans and the empirically calibrated output spectrum after extraction from the cube produced by the JWST pipeline.

3.3.3 Cross-Correlation

Snellen2014Simkin1974 Tonry1979 Petermann2019 Bodis2007 To quantify the similarity of the spectrum output by the JWST pipeline to the input into MIRISIM, we rely on the technique of cross correlation. For two arbitrary, complex-valued functions $f(t)$ and $g(t)$, we can compute the cross correlation as a function of the shift τ between the functions (typically in time or velocity space):

$$(f \star g)(\tau) \equiv \int_{-\infty}^{\infty} f^*(t)g(t + \tau)dt \quad (3)$$

Our signals of interest are astrophysical spectra, measured in a finite number of discrete wavelength bins. For such a signal with M bins:

$$(f \star g)[n] \equiv \sum_{m=0}^M f^*[m]g[m + n] \quad (4)$$

Care must be taken when cross-correlating signals, as differences in normalization can result in changes in the correlation coefficient. Our procedure takes in two spectra. The first is an emission spectrum produced by the petitRadTrans program **Molliere2019**, which provides our forward model with which we compare our data spectrum. Our data is the result of passing the

template spectrum through MIRISIM, and extracting it from the resulting detector image using the JWST pipeline. We then rebin the high-resolution input spectrum to the same wavelength bins as the data spectrum, using the `spectres` package. Prior to normalization, we remove any outliers from the spectrum (due to binning errors or instrumental effects) by setting any data points separater by more than 15 standard deviations from the mean to the median value of the spectrum. For each spectrum, we subtract the minimum value to remove any offset in the spectrum, and divide by the maximum value to restrict the range to $[0,1]$. We then use apply a Savitzky-Golay filter with a window of $1/4$ the length of the spectrum and a polynomial order of 3, which we then subtract from the unfiltered spectrum. This removes the continuum emission from the spectrum, and centers it around 0. We then renormalize the spectrum by dividing by the maximum absolute value such that the range is in $[-1,1]$. The cross correlation between the forward model and itself is computed, excluding the region of interest around 0 offset. This ‘autocorrelation’ is subtracted from the cross correlation between the forward model and the data spectrum in order to remove secondary peaks. Finally, we normalize the cross correlation by the standard deviation of the cross correlation (excluding the central peak), giving an output measured as a signal to noise ratio.

3.3.4 Residual Statistics

In addition to computing the cross correlation between the forward model and the data spectrum, we also examine the residuals between the two spectra. Here we can see any unexpected variations between the two (periodic signals, offsets or other features). We can also examine a histogram of the residuals, normalized by the standard deviation of the data spectrum. This provides us with a distribution which should have a mean of 0 and unit width if the data are unbiased and share a distribution with the true input spectrum.

3.4 FRINGING RESULTS

1. A stronger input signal results in a stronger correlation.
2. Fringing does NOT necessarily degrade the cross correlation SNR, but rather increases it. The scale of this increase seems to depend on the absolute magnitude of the correlation (ie, a larger increase at higher SNR)
3. The residuals from subtracting the template from the data has structure.
4. If the residuals are histogrammed (and normalized by the standard deviation of the data), the width of the distribution may correspond to the cross correlation SNR (wider distribution = lower SNR)
5. Only when strongly increasing the fringing effect does the SNR decrease.
6. Correcting for fringing using the standard JWST fringe map decreases the SNR when compared to the case of fringing with no correction, but is typically still above the no-fringing case.
7. The JWST correction performs worse in the off axis case, as the fringe pattern begins to vary more when compared to the CV fringing model.

3.4.1 Effects of fringing on spectral extraction

4

ATMOSPHERIC RETRIVALS

Everything photon of light that we receive from an exoplanet will interact with its atmosphere, and will therefore provide us with a hint of what that atmosphere may look like. An atmospheric retrieval is the process of reconstructing the atmosphere of an object based on an observed spectrum. This process relies heavily on having accurate models which can be parameterized by the physical quantities we are interested in: generally the temperature, pressure and composition (**Madhusudhan2018**). As these models cover a very large parameter space (>10 parameters, each covering several orders of magnitude), it is necessary to have an efficient method for sampling this space, computing a model and comparing this model to the data (**Benneke2012**).

This chapter will outline the process of an atmospheric retrieval from modelling to marginalization of posteriors, and will examine the impact that the instrumental effects described in chapter 3 have on the retrieved parameters. Additionally, this will provide an example of how the MIRI MRS can be used to explore exoplanet and brown dwarf atmospheres, and what observational parameters should be considered when studying these objects.

Schlawin2018 Fisher2019 Oreshenko2019 Barman2015 Benneke2013 Benneke2012 Blanco-Cuaresma2018 Konopacky2013

Morley2018 Lupu2018 Gandhi2018 Baudino2017 Line2013 Madhusudhan2018b Irwin2008 Robinson2016 Waldmann2015 Waldmann2015a Line2015; Line2017; Zalesky2019

Batalha2018 Feng2018 Molliere2019

4.1 ATMOSPHERIC MODELING

Atmospheric modelling is the task of creating an spectra based on the physical properties of the atmosphere. This is a broad task that can range from a 3D Global Circulation Model (GCM) which accounts for self-consistent atmospheric chemistry (**Chen2019**) to a 1D model based around an empirical temperature-pressure profile (**Molliere2019**). The choice of model depends largely on the requirements for accuracy and computational cost. Considering the potentially millions of possible atmospheres that must be examined in a retrieval problem, whatever model is used must be computationally efficient above all else.

Zhang2019

4.1.1 petitRADTRANS

For this work we chose to use the petitRADTRANS package due to its user-friendly python implementation, high speed computation for retrieval

Property	Description
Temperature	Parameterized, e.g. (Guillot2010)
Abundances	Parameterized, e.g. vertically constant
Scattering	Cloud scattering, transmission spectra only
Clouds	Power law and condensation clouds
Cloud particle size	f_{SED} and K_{ZZ} or parameterized
Particle size distribution	log-normal, variable width
Cloud abundance	Parameterized
Wavelength spacing	$R=1000$ (c-k), 10^6 (lbl)
Valid emission spectra	Clear, from NIR and longer

Table 5: Description of the parameters available in petitRADTRANS. For cloud particles, f_{SED} is the mass-averaged ratio of the cloud particle settling speed and mixing velocity. K_{ZZ} is the atmospheric eddy diffusion coefficient (Ackerman2001)

use and extensive high resolution, line-by-line spectral library for generating planetary spectra (Molliere2019). It is a 1D, radiative transfer package with many parameters options, described in table 5. PetitRADTRANS can compute both emission and transmission spectra, with an output spectral resolution of $R=1000$ in correlated k mode, or $R=1\,000\,000$ in line-by-line mode.

Note that much of the following sections applies to many other similar 1D radiative transfer atmospheric modelling programs such as ATMO (Goyal2018), Planetary Spectrum Generator (Villanueva2018), HELIOS (Malik2017; Malik2019) and others. Many (or even most) of these programs rely on the same set of high-resolution molecular line lists, including HITRAN/HITEMP (Rothman1973; Rothman2010; Gordon2017), ExoMol/ExoCross (Tennyson2016; Tennyson2016a; Yurchenko2018) and others. Behmard2019Guillot2010 Molliere2019

Radiative Transfer

In order to compute the emission spectrum an initial featureless black-body spectrum $B(T_{int})$ is passed through multiple discrete layers of the atmosphere, parameterized by their temperature, pressure, and the opacities of each of the species present in a given layer. Modelling each layer as plane parallel, the intensity is computed as in (Irwin2008; Molliere2017; Molliere2019)

$$I_{top} = B(T_{int})\mathcal{T}^{atmo} + \frac{1}{2} \sum_{i=0}^{N_L-1} \left[B(T^i) + B(T^{i+1}) \right] \left(\mathcal{T}^i - \mathcal{T}^{i+1} \right) \quad (5)$$

N_L is the number of layers in the atmosphere, and \mathcal{T} is the transmission from a given layer to the top of the atmosphere. All quantities are averaged per wavelength bin in c-k mode, while they are evaluated at each wavelength point in line-by-line mode.

Line-by-line

Correlated K

Goody1989 Lacis1991

Clouds

Line2016 Faherty2018 Morley2014

4.2 BAYESIAN METHODS

Lavie2017

4.2.1 MCMC

Foreman-Mackey2013 Speagle2019 MacKay2003

4.2.2 Nested Sampling

Skilling2004 Feroz2007 Feroz2008 Feroz2014 Feroz2019

4.2.3 multineest

Hyperparameters

4.2.4 Prior choice

4.2.5 Bayesian Model Selection

4.3 TARGETS

4.3.1 Atmospheric Parameters

Madhusudhan2012Moses2012Garland2019 Bowler2016 Fegley1994 Tokunaga1983

4.3.2 petitRadTrans

4.4 RESULTS

4.4.1 Posterior Distributions

5 | CONCLUSIONS

A | APPENDICES

A.1 PACKAGE REQUIREMENTS

```
numpy=1.4.0  
scipy=1.5
```